Applied Acoustics 236 (2025) 110754

Contents lists available at ScienceDirect

Applied Acoustics

journal homepage: www.elsevier.com/locate/apacoust

Slow waves in ducts with external SBH insertion and perforated boundaries

Sihui Li, Xiang Yu, Li Cheng *

Department of Mechanical Engineering, The Hong Kong Polytechnic University, Kowloon, Hong Kong, China

ARTICLE INFO

Keywords:
Sonic black hole
Duct acoustics
Wentzel-Kramers-Brillouin (WKB) solution
Acoustic silencer

ABSTRACT

An acoustic duct with external sonic black hole (E-SBH) insertion differs from the widely studied conventional configuration in which SBH components are located inside the duct. The E-SBH has the foreseeable benefit of avoiding flow obstruction inside the conduit while preserving the desired SBH effects. The characterizations of such SBH configurations alongside the wave propagation properties along the duct, however, have been less investigated. In this study, we analyze an E-SBH with perforation-modulated boundaries by means of theoretical, numerical and experimental methods. Wentzel-Kramers-Brillouin (WKB) solutions and their applicable ranges are first developed, allowing for a comprehensive characterization of slow-wave phenomena in both bare E-SBH and perforation-modulated E-SBH (PME-SBH) configurations. These solutions, verified against numerical simulations, provide a complete and analytical description of wave speed variations and define theoretical slow-wave limits for a given set of system parameters. By incorporating perforated boundaries and optimizing the perforation parameters, PME-SBH is shown to entail enhanced wave retarding effect, maintaining slow-sound with fewer inner rings. Finally, time-domain experiments confirm the predicted slow-wave effects in both external SBH configurations.

1. Introduction

Wave manipulation enables diverse intriguing and exotic functions that can be utilized in various engineering applications. Sonic black hole (SBH), as the acoustic counterpart to structural acoustic black hole (ABH) [1–4], has aroused significant research interest [5–10]. A conventional SBH structure consists of a series of rigid rings with power-law-reducing inner diameters installed within a duct of circular cross-section [11–13]. This basic one-dimensional configuration was first examined by Mironov, who theoretically predicted the slow-wave phenomenon for sound waves, analogous to that observed in structural ABH structures [13]. Upon entering an ideal SBH duct (where the inner diameter of the ring reduces to zero at the duct termination), the velocity of sound waves gradually decreases to zero, thus eliminating wave reflections [13,14]. However, achieving this ideal scenario is challenging due to the inevitable truncation of SBH. Most existing studies have primarily focused on the sound absorption performance of SBH structures and their optimization by adjusting the involved parameters [15–21]. Various methods have been developed for analyzing the physical properties of the SBH, including transfer matrix method (TMM) [22–24], modal decomposition method [25] and equivalent fluid method [26,27], etc. Recently, alternative SBH configurations, such as those with rectangular cross-sections, have also been studied [28–31]. Similar to structural ABHs, the acoustic benefits arise from the emergence of slow-wave effects [32,33]. Theoretical analyses and experimental validations have been carried out in both the frequency and time domains to confirm the slow-wave effects [14,34]. Furthermore, papers exploring the applications of SBH structures have begun to emerge gradually [35,36]. Collectively, these studies enhance our understanding of the underlying mechanisms in conventional SBH structures, providing useful guidance for the design and applications of SBH-based technology.

For the widely studied conventional SBH configurations, the inner diameter of the rings reduces along the duct length and becomes extremely small at the truncated end, thus jeopardizing the air-flow performance of the duct by creating significant fluid obstruction. To resolve this problem, a new type of SBH, referred to as the external sonic black hole (E-SBH), has been proposed, whose typical layout is illustrated in Fig. 1(a) [37]. Different from traditional SBHs, the E-SBH features a conduit with an externally mounted cone-shaped expansion chamber, housing a series of rigid inner rings. These rings have increasing outer diameters while maintaining constant inner diameters, flush-mounted along the inner surface of the duct. The E-SBH has the foreseeable benefit of being configured in such a way as to avoid flow

* Corresponding author.
E-mail address: li.cheng@polyu.edu.hk (L. Cheng).

https://doi.org/10.1016/j.apacoust.2025.110754
Received 25 February 2025; Received in revised form 7 April 2025; Accepted 18 April 2025
Available online 24 April 2025

obstruction inside the conduit while preserving the SBH effects. Recent studies have mainly evaluated the sound absorption performance of such structures, along with some design adjustments and parameter analyses [37,38]. The presence of slow-wave phenomena in the E-SBH structures was also briefly discussed [39,40]. Despite these works, research efforts on E-SBH are still largely insufficient as compared with those made on structural ABH, especially in terms of understanding and characterizing sound wave evolution as well as the convincing experimental validation of the slow wave phenomena. Moreover, our previous work demonstrated the benefit of introducing a perforation boundary (PB) into conventional SBH designs to effectively modulate their acoustic properties [14]. One legitimate question is how this practice might play out when PB is combined with E-SBH, which we refer to as perforation-modulated E-SBH (PME-SBH). As schematically shown in Fig. 1(b), this configuration necessitates a thorough investigation of the slow-wave phenomenon, as little has been done in terms of theoretical modelling, wave propagation properties and experimental confirmation. These research gaps motivate the present work.

This paper specifically investigates the wave propagation mechanisms in the proposed PME-SBH system, aiming to quantify the slow-wave effects and elucidate the benefits of incorporating PB. This study has three primary objectives thus showing its novelty: First, we establish WKB solutions for the E-SBH and PME-SBH with continuous or discrete admittance descriptions and evaluate their range of applicability. These solutions can be utilized to predict variations in acoustic velocity within the E-SBH or PME-SBH structures and to quantify the slow-wave limits, setting guidelines for further analyses and applications. These solutions are validated through numerical and experimental methods. Second, we elucidate the regulatory mechanism of the PB on the slow-wave effects in the PME-SBH, highlighting the advantages of incorporating PB. Finally, time-domain experiments are conducted for both configurations, enabling us to directly observe the slow-wave phenomenon in these retarding structures.

The rest of the paper is organized as follows. Section 2 derives the WKB solutions for the E-SBH and PME-SBH in two different cases, where both continuous and discrete admittance treatments are considered. The ranges of applicability for the analytical WKB solutions are also analyzed. Furthermore, the slow-wave limits of two specific models are also theoretically quantified. Section 3 begins by numerically determining the applicable range of WKB solutions for the E-SBH and verifying the accuracy of these solutions. Then, the influence of the geometrical parameters in the E-SBH on the slow-wave effect is discussed. Section 4 presents a verification of the WKB solutions for the PME-SBH, followed by an illustration of the influence of the perforation parameters on the slow-wave effects, which also demonstrates the benefits of the PB. Section 5 details the time-domain experiments and results on both E-SBH and PME-SBH configurations.

2. Theory

2.1. Governing equation

The governing equations for the E-SBH and PME-SBH structures are first derived. Fig. 2 provides schematic representations of the E-SBH structures in two distinct scenarios. Fig. 2(a) illustrates an E-SBH structure with a sufficiently large number of rings, where the admittance at the entrance of the backing cavity can be approximated as continuous. In contrast, Fig. 2(b) depicts the case where the E-SBH structure has a smaller number of rings, requiring the admittance to be treated as discrete. In both cases, the x-axis is chosen as the axis of symmetry in the waveguide.

In the harmonic regime, the generalized Webster equation for both cases writes [21,34]

$$p'' + p(k_0^2 + \frac{2Y\rho_0}{R_d}(i\omega)) = 0, \tag{1}$$

where p is the sound pressure; ρ_0 the air density; R_d the inner radius; Y the acoustic admittance at the entrance of the backing cavity; k_0 the wave number; i the imaginary unit and ω the angular velocity. Note that the governing equation of the E-SBH does not include a first-order differential term compared to that of the SBH derived in previous work [14]. This is because the inner diameter of the E-SBH remains constant. Also, note that the above equation form is general in the sense that different configurations require different Y. The corresponding solutions can then be utilized to predict the sound wave propagation inside the duct.

2.2. External SBH (continuous and discrete admittance treatments)

A bare E-SBH (without PB) is first analyzed analytically to elucidate the associated slow-wave effect. Two different scenarios are considered separately depending on the number of rings. For a large ring number, the admittance Y can be viewed as continuously varying along x direction, as shown in Fig. 2(a). As a result,

$$Y = (-i\omega)\frac{1}{\rho_0 c^2}\frac{R^2 + 2RR_d}{2R_d}, \tag{2}$$

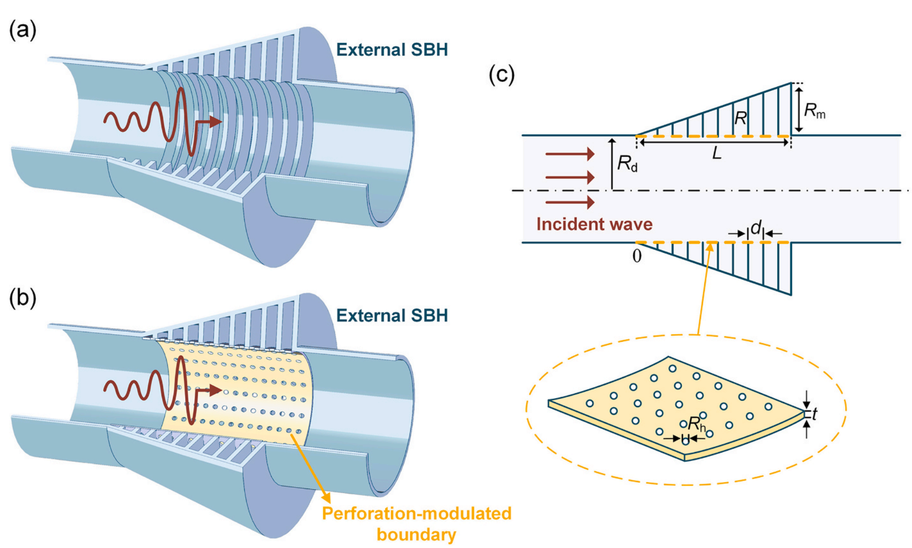

Fig. 1. Schematics of (a) an E-SBH and (b) a PME-SBH; (c) Cross-section of the PME-SBH showing its geometric and perforation parameters.

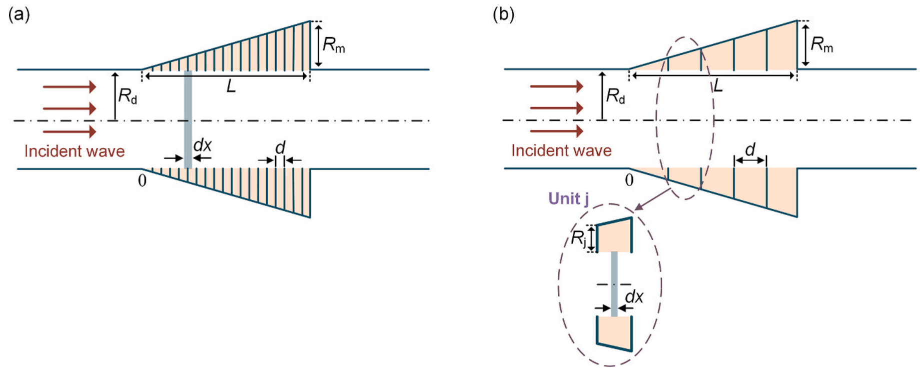

Fig. 2. Schematics of E-SBH configurations with (a) continuous varying admittance and (b) discrete varying admittance.

where R is the depth of the cavity varying with x. Substituting Eq. (2) into Eq. (1), the wave equation can be simplified as

$$p'' + p(k_0^2(\frac{R}{R_d}+1)^2) = 0. \tag{3}$$

WKB method is used to solve Eq. (3). The method imposes several requirements, and therefore the obtained solution is also limited to a certain range of applicability, which will be discussed in later sections. Assuming $p \sim e^{ik(x)x}$, the local wave number in the E-SBH writes

$$k(x) = k_0(\frac{R}{R_d}+1). \tag{4}$$

For a linear E-SBH with $R = R_m x/L$, where L is the length of the E-SBH and R_m the largest depth of the cavity,

$$k(x) = k_0 + k_0\frac{R_m x}{R_d L}. \tag{5}$$

Then, the local group velocity c_g and the sound propagation time T travelling from the inlet end to the position x can be deduced as

$$c_g = \left(\frac{\partial k}{\partial \omega}\right)^{-1} = \frac{c}{\frac{R_m x}{R_d L}+1}, \tag{6}$$

$$T = \frac{1}{c}(x + \frac{R_m x^2}{2R_d L}). \tag{7}$$

Consequently, the total time taken for the wave to pass through the entire linear E-SBH is

$$T_{total} = \frac{L}{c}(1+\frac{R_m}{2R_d}). \tag{8}$$

From Eq. (8), it is evident that the slow-wave phenomenon occurs since$T_{total} > L/c$, which is the nominal time required for the wave to propagate freely through the same trajectory. Notably, for a given geometrical variation of the ring's outer diameter (linear in the present case), the resultant slow-wave effect in E-SBH is solely determined by R_m/R_d, a ratio between the inner radius of the duct and the largest depth of the E-SBH cavity. Since this ratio R_m/R_d cannot be infinite, the speed of sound waves in the E-SBH can never reach zero, meaning an ideal and perfect black hole effect can never be realized. Therefore, for a given E-SBH structure, there exists a limit to govern how much the sound waves can be slowed down. For example, if $R_m = R_d$, $T_{total} = 3L/2c$, this indicates that the propagation time can only increase to 1.5 times that of the nominal case of free propagation. In other words, this E-SBH slows down the sound waves by a factor of 1.5 on average. Similarly, for a quadratic E-SBH, $R = R_m(1-(L-x)^2/L^2)$,

$$k(x) = k_0 + k_0\frac{R_m(1-\frac{(L-x)^2}{L^2})}{R_d}. \tag{9}$$

One then has

$$c_g = \frac{cR_d}{R_m(1-\frac{(L-x)^2}{L^2})+R_d}, \tag{10}$$

$$T = \frac{R_m}{cR_d}(x+\frac{(L-x)^3}{3L^2}-\frac{L}{3})+\frac{x}{c}, \tag{11}$$

$$T_{total} = \frac{L}{c}(1+\frac{2R_m}{3R_d}). \tag{12}$$

It is clear that for the same radius ratio of $R_m = R_d$, $T_{total} = 5L/2c$, this results in 1.67 times increase in propagation time. This suggests that better SBH effects can be realized by quadratic profile compared to its linear counterpart, suggesting a possible way to optimize SBH profile for enhanced slow-wave effects.

In the case of E-SBH with a small number of rings, the admittance Y can no longer be regarded as continuously varying. We assume that Y at the entrance of each cavity is uniformly distributed. As shown in Fig. 2 (b), the E-SBH can be discretized into N units, each comprising a backing cavity and the inner duct region. In a given unit j, Y can be acquired as

$$Y = (-i\omega)\frac{1}{\rho_0 c^2}\frac{V_j}{S_j}, \tag{13}$$

where S_j is the area at the entrance of the cavity of the unit; $V_j = \pi d\left((R_j+R_d)^2 - {R_d}^2\right)$, which is the corrected cavity volume, where d is the thickness of the unit and R_j the depth of the cavity. Substituting Eq. (13) into Eq. (1) yields

$$p'' + p(k_0^2(1+\frac{2V_j}{S_j R_d})) = 0. \tag{14}$$

Then, by applying the WKB method, the local wave number at the unit j can be written as

$$k_j = k_0\sqrt{(1+\frac{2V_j}{S_j R_d})}. \tag{15}$$

This leads to

$$c_{g-j} = \frac{c}{\sqrt{\left(1+\frac{2V_j}{S_j R_d}\right)}}, \tag{16}$$

$$T = T_1 + T_2 + \ldots + T_{j-1} + \int_{x_j}^{x}\frac{1}{c}\sqrt{\left(1+\frac{2V_j}{S_j R_d}\right)}dx, \tag{17}$$

where x_j is the coordinate of the inlet end of the unit j; T_j the time elapsed during the propagation of the wave through the unit j.

The range of applicability for the WKB solution in Eq. (4) is established. The WKB approximation is applicable only if the coefficients in the wave equation (Eq. (3)) vary slightly within one wavelength. Hence, the following inequality needs to be satisfied,

$$\left|\frac{d(k_0^2(\frac{R}{R_d}+1)^2)}{dx}\frac{1}{k}\right| \ll \left|k_0^2(\frac{R}{R_d}+1)^2\right|. \tag{18}$$

Equation (18) can be simplified as

$$(R+R_d)^2 k_0 - 2R' R_d \gg 0. \tag{19}$$

This condition should be satisfied for the entire variation range of x between 0 and L. For a linear E-SBH with $R = R_m x/L$, Eq. (19) can be simplified into

$$C_1 = R_d^2 k_0 - 2\frac{R_m}{L} R_d \gg 0. \tag{20}$$

In subsequent simulations, using Eq. (20), specific applicable parameter ranges can be determined for a given E-SBH structure. The WKB solution is established as a modelling method for the E-SBH, which will be validated later by means of simulation and experimentation.

2.3. External SBH with perforation-modulated boundary

Consider now an E-SBH with a perforation-modulated boundary, namely PME-SBH. Similarly, depending on the number of rings, both discrete and continuous treatments of Y at the PB can be applied. In either case, the surface impedance Z at the PB is the addition of the acoustic impedance of the perforated sheet and that of the backing cavity. For the continuous treatment, which is applicable in cases with a large number of rings, one has

$$Z = \frac{2\rho_0 c^2 R_d}{(-i\omega)(R^2+2RR_d)} - (\frac{4t}{R_h}+4)\frac{R_s}{\varphi} - i\frac{\omega\rho_0}{\varphi}(2\varepsilon_e+t) - i(\frac{4t}{R_h}+4)\frac{R_s}{\varphi}, \tag{21}$$

$$R_s = \frac{1}{2}\sqrt{2\eta\omega\rho_0}, \tag{22}$$

$$\varepsilon_e = 0.48\sqrt{\pi R_h^2}(1-1.47\sqrt{\varphi}+0.47\sqrt{\varphi^3}), \tag{23}$$

in which t is the thickness of the PB; R_h the hole diameter of the PB; φ the perforation ratio of the PB; η the dynamic viscosity of air. Note that the first term in Eq. (21) represents the impedance of the backing cavity, derived from Eq. (2). The remaining three terms correspond to Beranek Ingard's impedance model for the PB sheet [41]. The validity of this model and its advantages have been discussed in our previous work [34]. R_s in Eq. (22) denotes the surface resistance. ε_e in Eq. (23) represents a correction length, which is a function of the perforation ratio and the hole diameter of the PB.

The surface admittance at the PB then writes

$$Y = \frac{1}{Z} = \frac{1}{A+iB}, \tag{24}$$

where

$$A = -(\frac{4t}{R_h}+4)\frac{R_s}{\varphi}, \tag{25}$$

$$B = \frac{2\rho_0 c^2 R_d}{\omega(R^2+2RR_d)} - \frac{\omega\rho_0}{\varphi}(2\varepsilon_e+t) - (\frac{4t}{R_h}+4)\frac{R_s}{\varphi}. \tag{26}$$

Substituting Eq. (24) into Eq. (1) yields the wave equation in compact form as

$$p'' + p(k_0^2 + \frac{2\rho_0\omega}{R_d(B-iA)}) = 0. \tag{27}$$

Applying WKB method to Eq. (27) results in the local wave number $k(x)$ expression as

$$k(x) = \sqrt{k_0^2 + \frac{2\rho_0\omega}{R_d(\frac{2\rho_0 c^2 R_d}{\omega(R^2+2RR_d)} - \frac{\omega\rho_0}{\varphi}(2\varepsilon_e+t) - (\frac{4t}{R_h}+4)\frac{R_s}{\varphi} + i(\frac{4t}{R_h}+4)\frac{R_s}{\varphi})}}. \tag{28}$$

The local velocity c_g and the propagation time T can be derived from Eq. (28). For a linear PME-SBH with $R = R_m x/L$,

$$k(x) = \sqrt{k_0^2 + \frac{2\rho_0\omega}{R_d(\frac{2\rho_0 c^2 R_d L^2}{\omega R_m x(R_m x+2R_d L)} - \frac{\omega\rho_0}{\varphi}(2\varepsilon_e+t) - (\frac{4t}{R_h}+4)\frac{R_s}{\varphi} + i(\frac{4t}{R_h}+4)\frac{R_s}{\varphi})}}. \tag{29}$$

For a PME-SBH structure with a small number of rings, only the first term in Eq. (21) needs to be changed, which can be easily derived from Eq. (13). For the unit j, the above procedure leads to the surface impedance Z_j at the PB as

$$Z_j = \frac{Z_0 S_j}{k_0 V_j} i - (\frac{4t}{R_h}+4)\frac{R_s}{\varphi} - i\frac{\omega\rho_0}{\varphi}(2\varepsilon_e+t) - i(\frac{4t}{R_h}+4)\frac{R_s}{\varphi}, \tag{30}$$

where Z_0 is the characteristic impedance, $\rho_0 c$; R_s and ε_e are given as Eq. (22) and Eq. (23), respectively. Similarly, cast Y_j into the following compact form

$$Y_j = \frac{1}{Z_j} = \frac{1}{A_j+iB_j}, \tag{31}$$

with

$$A_j = -(\frac{4t}{R_h}+4)\frac{R_s}{\varphi}, \tag{32}$$

$$B_j = \frac{Z_0 S_j}{k_0 V_j} - \frac{\omega\rho_0}{\varphi}(2\varepsilon_e+t) - (\frac{4t}{R_h}+4)\frac{R_s}{\varphi}. \tag{33}$$

The simplified wave equation applied to each unit becomes

$$p'' + p(k_0^2 + \frac{2\rho_0\omega}{R_d(B_j-iA_j)}) = 0. \tag{34}$$

The WKB solution of the above equation gives the local wave number k_j for unit j as

$$k(x)_j = \sqrt{k_0^2 + \frac{2\rho_0\omega}{R_d(\frac{Z_0 S_j}{k_0 V_j} - \frac{\omega\rho_0}{\varphi}(2\varepsilon_e+t) - (\frac{4t}{R_h}+4)\frac{R_s}{\varphi} - (\frac{4t}{R_h}+4)\frac{R_s}{\varphi}i)}}. \tag{35}$$

The corresponding group velocity can then be readily obtained, along with the total travelling time for sound waves to pass through the SBH portion by aggregating the travelling times of all units, similarly as Eq. (17). The range of applicability for the above WKB solution Eq. (28) can also be determined by following the same approach as Eqs. (18) and (19) (with detailed analytical expressions omitted here for briefness). For a linear PME-SBH with $R = R_m x/L$, the WKB condition to be fulfilled can also be written in the form of Eq. (20),

$$C_2 = |k| - \frac{-\frac{4\rho_0 c^2 L^2 R_d(LR_d+R_m x)}{\omega R_m x^2(2LR_d+R_m x)}}{\frac{2\rho_0 c^2 L^2 R_d}{\omega R_m x(R_m x+2R_d L)} - \frac{\omega\rho_0}{\varphi}(2\varepsilon_e+t) - (\frac{4t}{R_h}+4)\frac{R_s}{\varphi} + i(\frac{4t}{R_h}+4)\frac{R_s}{\varphi}} \gg 0. \tag{36}$$

By now, the full set of analytical WKB solutions for both bare and PB-modulated E-SBH cases has been obtained. The validation and the application range of each case will be examined later. This set of analytical tools will be used, in conjunction with numerical simulations and experiments, to elucidate the physical process associated with slow-wave propagation inside the ducts.

3. Numerical simulations and analyses

3.1. External sonic black hole without PB

3.1.1. Validation of the WKB solutions

To ensure the accuracy of the WKB solution for the E-SBH, the structural parameters must satisfy the WKB condition specified in Eq. (19). Assuming a linear E-SBH with $R = R_m x/L$, the applicable ranges for its geometrical parameters R_m and L are first determined. In the numerical example, R_d is set to 0.05 m. Considering the practical applications of this structure, the variation ranges of R_m and L are chosen to be from 0 to 0.1 m and 0 to 0.3 m, respectively. Using Eq. (20), the values of C_1 are calculated for various E-SBH configurations, with results presented in Fig. 3(a) and Fig. 3(b) for 1000 Hz and 1500 Hz (Lower than the cut-off frequency of the waveguide), respectively. In these figures, the yellow regions represent the parameter ranges that satisfy the condition for using Eq. (20), delineating the validity range of the WKB solution. Outside this region (green areas), WKB solutions for E-SBH become inaccurate and cannot be utilized. Notably, the validity range expands with increasing frequency, which is consistent with the assumption made on WKB. Overall, the WKB solution is valid across a large variable space, especially at higher frequencies. It is worth noting that as the WKB solutions are derived based on the plane wave assumption, the valid frequency range of the WKB solutions needs to be below the cut-off frequency of the duct.

Next, the accuracy of the WKB method in predicting the slow-wave phenomenon in the E-SBH is verified. Here, the results obtained using the FEM serve as baselines for validating the WKB solutions. These FEM simulations are conducted using COMSOL Multiphysics, where transient simulations to portray wave propagation in specific E-SBH configurations are carried out. The parameters used in the selected linear E-SBH cases are detailed in Table 1. The E-SBH has 29 rigid rings (i.e. 30 cavities), which is sufficient to justify the continuous admittance treatment. An incident plane wave is defined at the entrance of the duct, which is filled with air with $\rho_0 = 1.215$ kg/m^3 and $c = 340$ m/s.

Table 1
Geometric parameters of the E-SBH.

	R_d (m)	R_m (m)	L (m)
E-SBH	0.05	0.04	0.15

Damping loss in the E-SBH structure is considered by using a complex sound speed $c = 340 \times (1 + 0.01i)$ m/s. The center frequency of the input burst signal is set as 1000 Hz. A perfectly matched layer is added to the exit end of the duct to eliminate wave reflections.

Using the time-domain transient simulation, the sound pressure distribution along the center axis of the E-SBH at each time instant can be obtained. By tracing the first wave peak in the waveform at each time step, the relationship between its arrival position and time can be determined, which is plotted in Fig. 3(c). The position-time curve obtained from the WKB solution (Eq. (7)) is also included in Fig. 3(c). The orange-highlighted area, delineated by the orange dotted line, represents the E-SBH region. The close agreement between WKB and FEM results in Fig. 3(c) verifies the accuracy of the WKB solutions, demonstrating their effectiveness in analytically quantifying slow-wave propagations within the E-SBH structure. The slight differences between these two sets of results at the exit of the E-SBH ($x = 0.15$ m) are attributed to the unavoidable error caused by the presence of reflected waves in the FEM. Since the slopes of the curves represent the local velocity, it can be seen from Fig. 3(c) that the local velocity gradually decreases in the E-SBH region, evidencing the slow-wave phenomenon within this structure.

The configuration with a reduced number of rings, specifically 9, is also examined. Using Eq. (17) for the discrete admittance treatment, the WKB results remain consistent with the FEM results, further validating the WKB solutions (figures omitted here for conciseness).

3.1.2. Slow wave phenomenon and parametrical influence

The above comparisons show that the obtained WKB solutions can be utilized to describe the sound wave propagation in the E-SBH models,

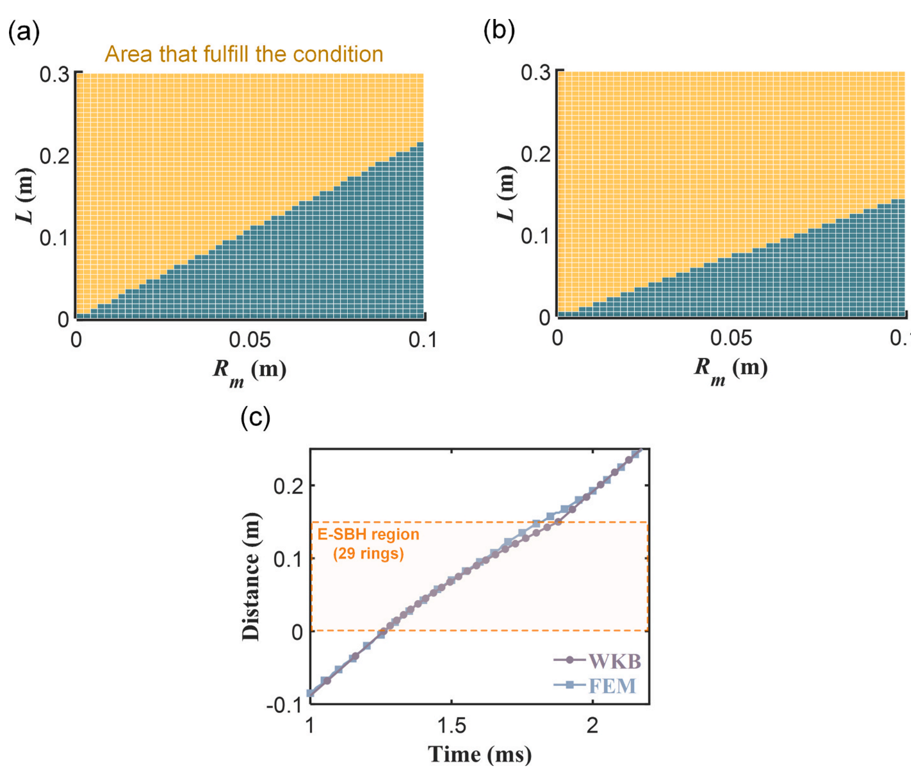

Fig. 3. The applicable range of parameters for using the WKB solutions for the E-SBH configuration at (a) 1000 Hz and (b) 1500 Hz; (c) Wavefront location versus time curves for a 29-ring E-SBH.

irrespective of the number of rings. Furthermore, the observed slow-wave phenomenon is not very pronounced in the bare E-SBH configuration.

The degree of slow-sound can be adjusted through proper parametric tuning. To investigate this, the verified WKB solution in Eq. (6) is employed to calculate the variation in sound velocity across different configurations. Two major parameters, R_m/R_d and L, are studied. Firstly, using the same L value tabulated in Table 1, R_m/R_d is selected as 0.25, 0.5, 1, 2 and 4, respectively. The local group velocities within these E-SBH configurations are plotted and compared in Fig. 4(a). Note that the region from $x = 0$ to $x = 0.15$ m represents the E-SBH region. As shown in Fig. 4(a), the sound velocity decreases more rapidly with a larger R_m/R_d, also leading to a lower minimum velocity value. Hence, the slow wave limit can be extended by increasing the ratio of R_m/R_d, at the expense of increasing the expansion ratio and ending up with a bulkier E-SBH structure. Then the influence of L on the slow-wave effect is also investigated by varying L from 0.05 m, 0.1 m, 0.15 m, 0.2 m to 0.25 m. In this case, R_m/R_d is fixed at 1. Similarly, by using Eq. (6), the local group velocities in these new configurations are presented and compared in Fig. 4(b). In the figure, the increase in L also impacts the sound velocity distribution inside the duct. However, in all these E-SBH models, the velocities of the sound wave decrease from 340 m/s to 170 m/s reaching the E-SBH termination. Therefore, R_m/R_d is the primary factor determining the slow wave effect, providing an important guideline for the design of E-SBH.

3.2. External sonic black hole with perforation-modulated boundary

3.2.1. Validation of the WKB solutions

We now focus on the E-SBH structure with perforation-modulated boundary, PME-SBH. The WKB solutions for the PME-SBH configuration are validated, along with the determination of the applicable range of the solutions. The influence of the PB parameters on the slow-wave effect is also elucidated. Furthermore, the benefits of inserting PB into E-SBH structure are demonstrated.

The applicable range of the perforation parameters R_h and φ in the PME-SBH is determined first. Note that the ranges of R_m and L that satisfy the WKB condition Eq. (36) do not change much compared to Fig. 3 (a) and (b) in the case where different R_h and φ are considered. Thus, according to these two figures, R_m and L are selected and shown in Table 2. Since the thickness t of the PB in the PME-SBH does not vary over a wide range, an appropriate value is set, 0.4 mm. R_h and φ, as variables, are varied from 0.2 mm to 3 mm and from 1 % to 60 %, respectively. C_2 in Eq. (36) is calculated for the PME-SBH configurations for different R_h and φ, as shown in Fig. 5 (a). The brown region represents the applicable parameter range where C_2 is greater than zero and the WKB condition is satisfied. Hence, R_h and φ in the subsequent simulations are selected as 1 mm and 40 %, which are picked from the brown region. Again, we note that the validation range covers a large portion of the R_h and φ variation range, nearly all perforation hole parameters (from micro- to macro) provided the perforation ratio is roughly larger than 8 %.

Table 2
Parameters of the PME-SBH.

	R_d (m)	R_m (m)	L (m)	t (mm)	R_h (mm)	φ (%)
PME-SBH	0.05	0.04	0.15	0.4	1	40

Similarly, the accuracy of the WKB method for the PME-SBH with both a large (29) and small (9) number of rings is verified. FEM is still used as a reference method for validating the WKB results. The plots of propagation distance versus time for both configurations are shown in Fig. 5(b) and (c), respectively, using the same approach as Section 3.1.1. We can again notice a nice agreement between WKB solutions and the FEM results, suggesting that WKB solutions can indeed be used as a predictive tool for the quantification of the slow-wave phenomena in the PME-SBH configurations.

3.2.2. Perforation-modulated slow wave phenomenon

In this section, the regulatory mechanism of the perforated boundary (PB) on slow wave effects in a PME-SBH is studied. Meanwhile, the potential benefits of adding PB on top of the above E-SBH are demonstrated. Firstly, using the 29-ring configuration, the effect of modulating perforation parameters, φ and R_h on the slow wave effect is shown. Using COMSOL again, transient simulations on a large number of PME-SBH configurations with different R_h and φ are conducted. For these 29-ring PME-SBHs, φ is taken from 1 % to 60 % at 2 % intervals, and R_h is selected from 0.2 mm to 3 mm at 0.1 mm intervals. By randomly combining these two parameters, 870 configurations can be yielded. The other parameters are the same as those in Table 2. Through transient simulations, the propagation time of the sound wave from the entrance to the exit of these PME-SBH models can be calculated. The ratio of the propagation time T in the PME-SBH retarding structures to the time T_0 of a wave travelling freely over the same distance is shown in Fig. 6(a). A larger ratio T/T_0 pinpoints better slow-wave performance. From Fig. 6 (a), it is clear that φ of the PB has the greatest impact on the slow-wave effects. The results of all PME-SBH configurations with $R_h = 1$ mm are highlighted in Fig. 6(a) and plotted in Fig. 6(b). These models have a constant R_h, with only φ varying from 1 % to 60 %. Furthermore, the results of T/T_0 calculated by the WKB method are also displayed in Fig. 6 (b). The WKB results agree well with the FEM results, with differences only when φ is small (parameter range where the WKB condition is not satisfied). From Fig. 6(b), it can be found that when φ is very small (about 1 % ~ 5 % in this case), the slow wave effect is very weak. As φ increases (about 5 % ~ 10 %), the slow wave effect gradually improves, persistent when φ continues to increase (about 10 % ~ 40 %). Finally, an exceedingly large φ (about 40 % ~ 60 %) slightly worsens the slow wave effect. Fig. 6(e) reveals the reason why φ has a significant effect on the

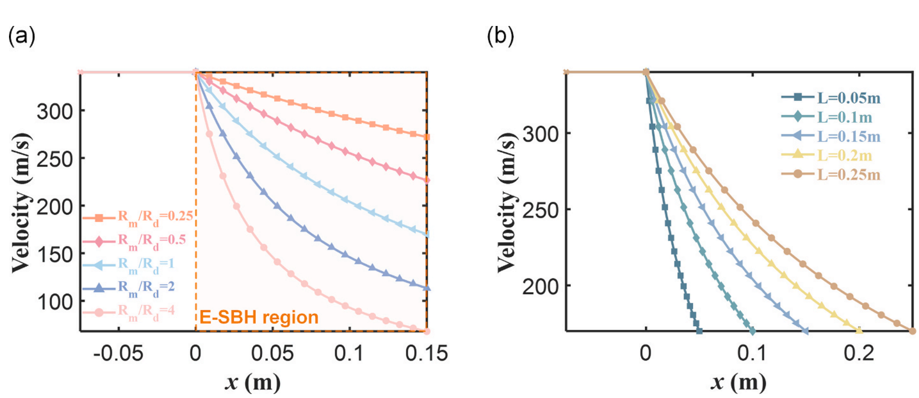

Fig. 4. Local group velocities within the E-SBH configurations with different (a) R_m/R_d(0.25, 0.5, 1, 2 and 4) or (b) L(0.05 m, 0.1 m, 0.15 m, 0.2 m and 0.25 m).

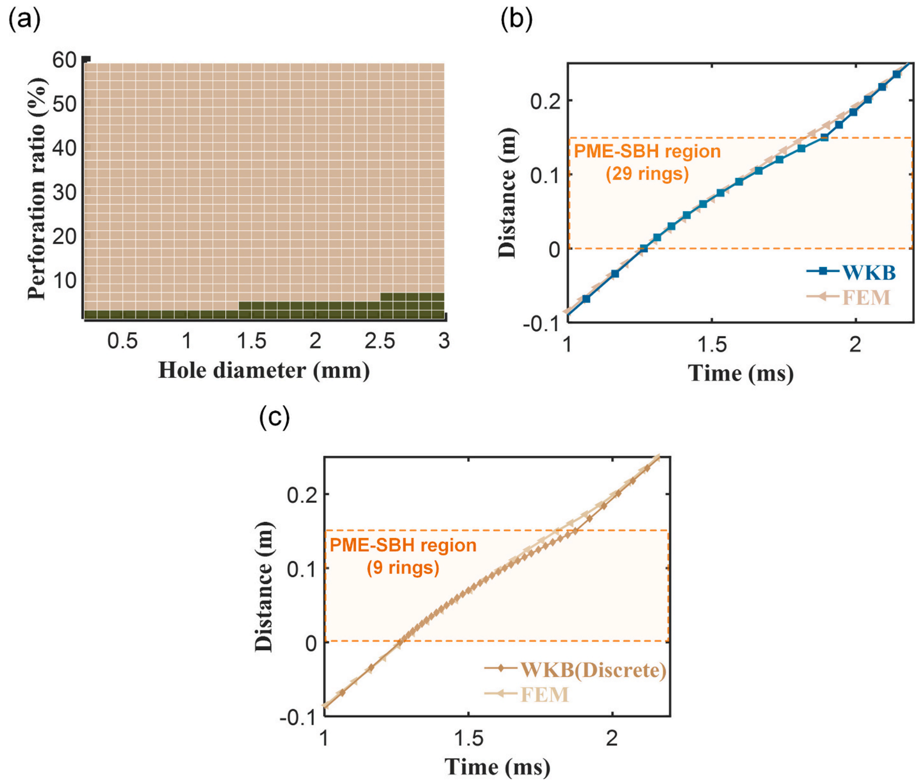

Fig. 5. (a) Applicability range of PB parameter of the PME-SBH configuration at 1000 Hz; Wavefront location versus time curves for (b) a 29-ring PME-SBH and (c) a 9-ring PME-SBH.

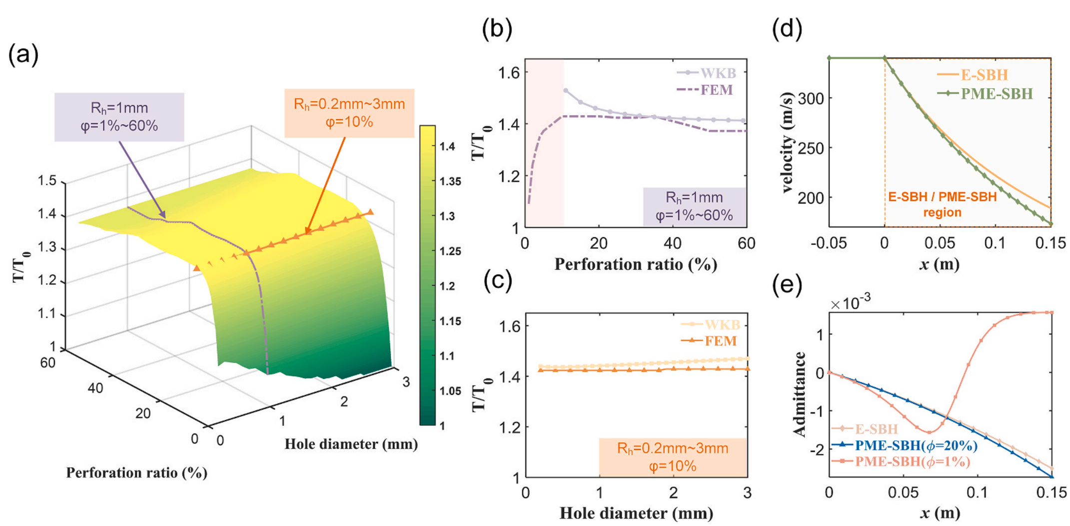

Fig. 6. (a) T/T_0 of the 29-ring PME-SBH configurations with different R_h and φ; T/T_0 of all PME-SBH configurations with (b) $R_h = 1$ or (c) $\varphi = 10$ %; (d) velocity variations within the bare E-SBH and the PME-SBH ($\varphi = 20$ %, $R_h = 0.2$ mm); (e) admittance distribution at the entrance of the backing cavity in the E-SBH and two PME-SBH models.

slow wave effect. The distribution of admittance along the axial direction at the entrance of the backing cavity in the bare E-SBH and two PME-SBH configurations ($\varphi = 20$ % and $\varphi = 1$ %) are given in Fig. 6(e), respectively. Obviously, continuously and monotonically varying admittance results in a good slow-wave effect. On the contrary, when $\varphi = 1$ %, the admittance no longer varies monotonically, resulting in deteriorated slow-wave effects. To conclude, φ can significantly affect the admittance within the retarding structure, thereby impacting the slow-wave effect.

Fig. 6(a) also implies that R_h has little effect on the slow wave effect. Similarly, T/T_0 of all PME-SBH configurations with $\varphi = 10$ % is highlighted in Fig. 6(a) and plotted in Fig. 6(c), alongside the WKB results. In Fig. 6(c), these two results match well and the WKB solution is applicable regardless of R_h. Also, it is clear that the slow wave effect remains constant as R_h increases (0.2 mm ~ 3 mm). Note that, in Fig. 6(a), the effect deteriorates as R_h increases only when φ is very small (e.g. 1 %). But such extremely small values of φ are not our focus. Thus, φ is the primary factor to consider when designing effective PME-SBH.

The next question is whether the inclusion of a PB sheet is conducive to increasing the slow-wave performance in an E-SBH. To illustrate this, the variation of the velocity of a 1000 Hz sound wave in an E-SBH and a PME-SBH is calculated using the WKB method and compared in Fig. 6(d). PME-SBH has the PB parameters $\varphi = 20$ % and $R_h = 0.2$ mm. Fig. 6(d) shows the sound wave decelerate more rapidly in the PME-SBH. Moreover, the velocity of the sound wave can be reduced to a lower level within the PME-SBH, specifically to roughly 170 m/s at the exit of the SBH section. While, in the E-SBH, the velocity can only be decreased to about 190 m/s. Therefore, the slow wave performance in the E-SBH can be enhanced by inserting the PB with appropriate perforation parameters, showing the appealing benefit of the PB.

Also note that a large number of rigid rings is usually required in the bare E-SBH structure, which inevitably adds cost and hampers practical applications. The inclusion of the PB offers the possibility of simplifying the structural design using a reduced number of rings while maintaining the excellent slow wave effect. To illustrate this, T/T_0 variation on 870 PME-SBH configurations is obtained by conducting the time-domain transient simulations, shown in Fig. 7(a). These configurations have the same parameters as those in Fig. 6(a), except the number of rings is reduced to 9. The results of all configurations with $R_h = 1$ mm are plotted in Fig. 7(b). For better comparison, the results of the 29-ring PME-SBHs in Fig. 6(b) are also presented in Fig. 7(b). We can see that the slow-wave effect in the 9-ring PME-SBHs still remains excellent within a specific φ range (indicated by the blue area in Fig. 7(b)), specifically from $\varphi = 5$ % to $\varphi = 10$ %, within which the observed slow-wave effect is as good as that in the 29-ring PME-SBHs. However, when φ is large (about 15 % ~60 %), the slow-wave effect in the 9-ring PME-SBHs deteriorates and becomes worse than that in the 29-ring models. Hence, inserting PB with a properly chosen perforation ratio allows for maintaining an appreciable slow-wave effect even when the number of rings is reduced. Finally, using the WKB solution Eq. (35), the sound velocity variation in a 9-ring E-SBH and PME-SBH are shown in Fig. 7(c). For the latter, $\varphi = 10$ %, $R_h = 0.2$ mm. It can be seen that the PME-SBH outperforms the E-SBH in terms of wave retarding effect.

4. Experimental assessment

Experiments are performed to confirm the observed slow wave phenomena in the theoretical analyses, as well as the validity of the WKB solutions. The experimental set-up used in the tests is illustrated in Fig. 8, which can be divided into several components, as shown in Fig. 8(a). A speaker (Fig. 8(b)) is installed on the left end of the duct to generate a five-cycle burst sound wave at the frequency of 1000 Hz, consistent with previous simulations. The measurement system comprises a fixed reference microphone (Fig. 8(c)), placed 20 cm from the entrance of the SBH sample, and a measuring microphone that is continuously moved along the duct. The movable microphone (Fig. 8(a)) is a MEMS microphone fixed to one end of a thin carbon fiber rod, with the other end attached to an automatically driven sliding rail. The installation of the SBH sample is shown in Fig. 8(a) and (c). Four different linear SBH configurations (Fig. 8(f), (g) and (h), 29-ring and 9-ring E-SBHs, 29-ring and 9-ring PME-SBHs) are tested. The E-SBH samples are manufactured by 3D printing using resin. Note that the ends of the E-SBHs are designed to fit the impedance tubes. The geometric parameters of the E-SBHs are presented in Fig. 8(e). The rings are 1.5 mm thick and equally spaced. The PME-SBHs share the same layout as the E-SBHs. The perforated sheet used in the PME-SBHs is made of steel with perforation parameters chosen as $\varphi = 35$ %, $R_h = 1$ mm. Fig. 8(h) illustrates a PME-SBH specimen used in the experiments.

The measurement procedure is briefly introduced here. The burst sound signal emitted by the speaker is captured by both the reference and movable microphones. This allows the measurement of the waveforms at these two locations, allowing for the extraction of the time taken for the sound wave to pass through by tracing the signal peaks in the time-domain. The curves showing the propagation distance of the wavefront and propagation time can be acquired by moving the moveable microphone to different positions, where the distance is precisely controlled by the automatic slide rail. In the experiment, the slide rail advances in increments of 4 mm, with a 5-second pause at each location to ensure stable and low-noise measurements. The total length of the slide rail is 400 mm. Hence, measurements are conducted at 100 discrete points to obtain the distance curves versus time, whose slopes represent the local sound velocity both inside and outside the SBH portion.

Experimental results on all four specimens are given in Fig. 9, alongside WKB and FEM solutions. Comparisons among the three sets of results show good agreement. Furthermore, within the E-SBH or PME-SBH regions bounded by the two dotted lines, the curves all bend to different extents, suggesting reduced slopes and, therefore, a reduced sound speed inside the SBH portion. Similar to the theoretical and numerical analysis part, we did not try to optimize the system to achieve the best possible slow-wave performance, which is basically a design and optimization issue. Instead, we focus on the development of predictive tools, as well as the understanding and assertion of the sound

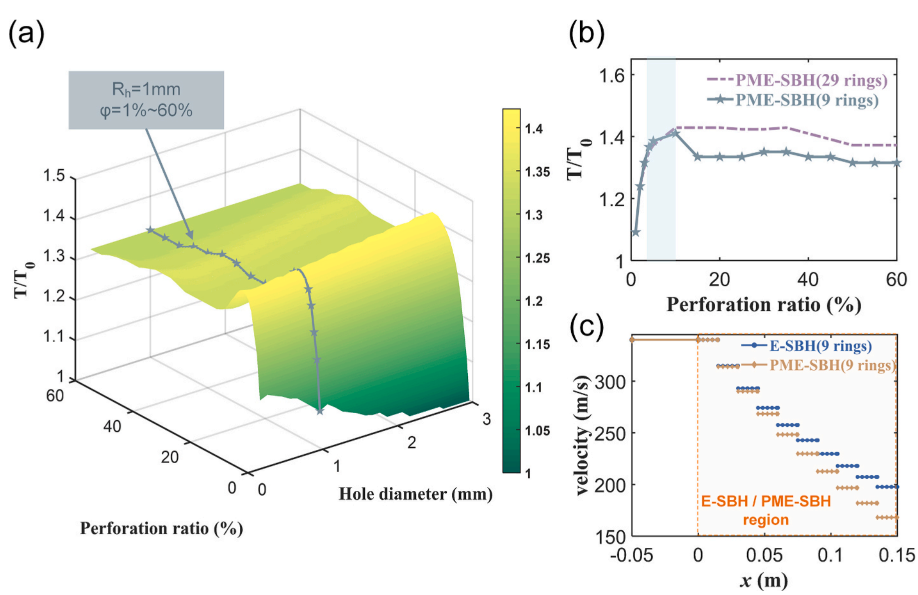

Fig. 7. (a) T/T_0 of the 9-ring PME-SBH configurations with different R_h and φ; (b) T/T_0 of all 9-ring and 29-ring PME-SBH configurations with $R_h = 1$; (c) velocity variations within the 9-ring E-SBH and 9-ring PME-SBH.

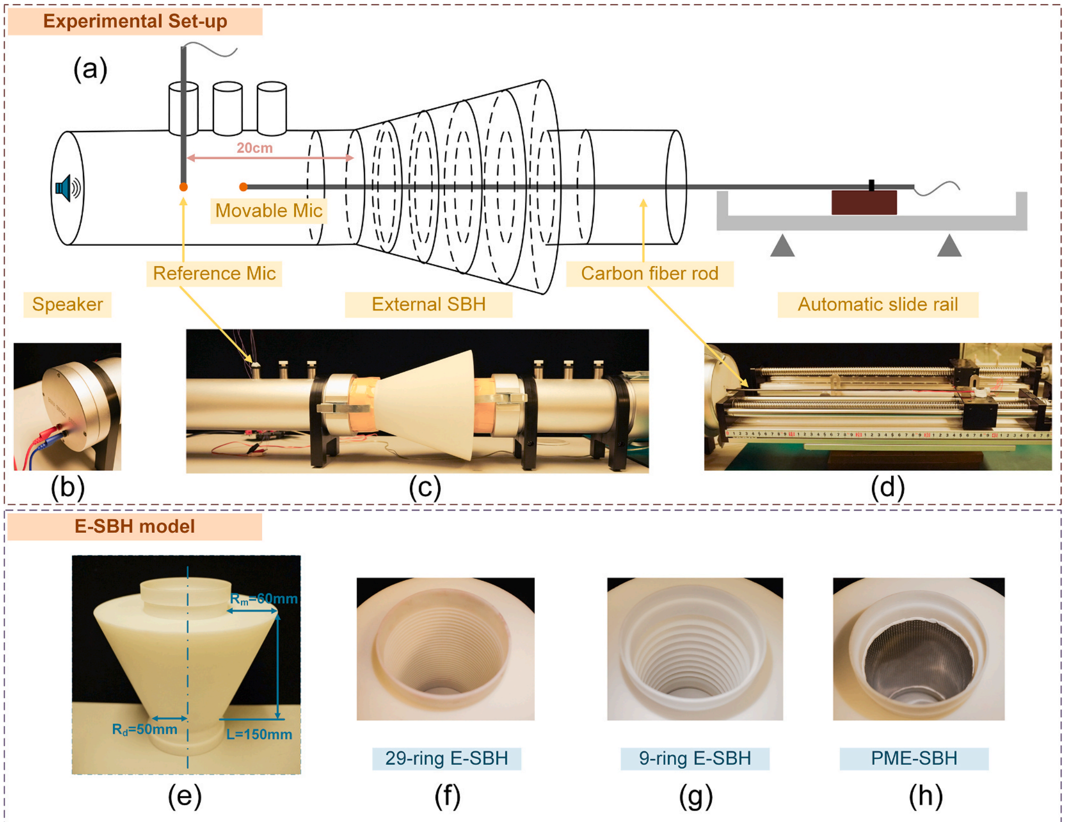

Fig. 8. (a) Schematic of the experimental set-up; (b) Speaker in the experiment; (c) Fixed reference microphone and the tested model; (d) Automatic slide rail; (e) Parameters of the E-SBH; (f) 29-ring E-SBH model; (g) 9-ring E-SBH model; (h) 29-ring or 9-ring PME-SBH model.

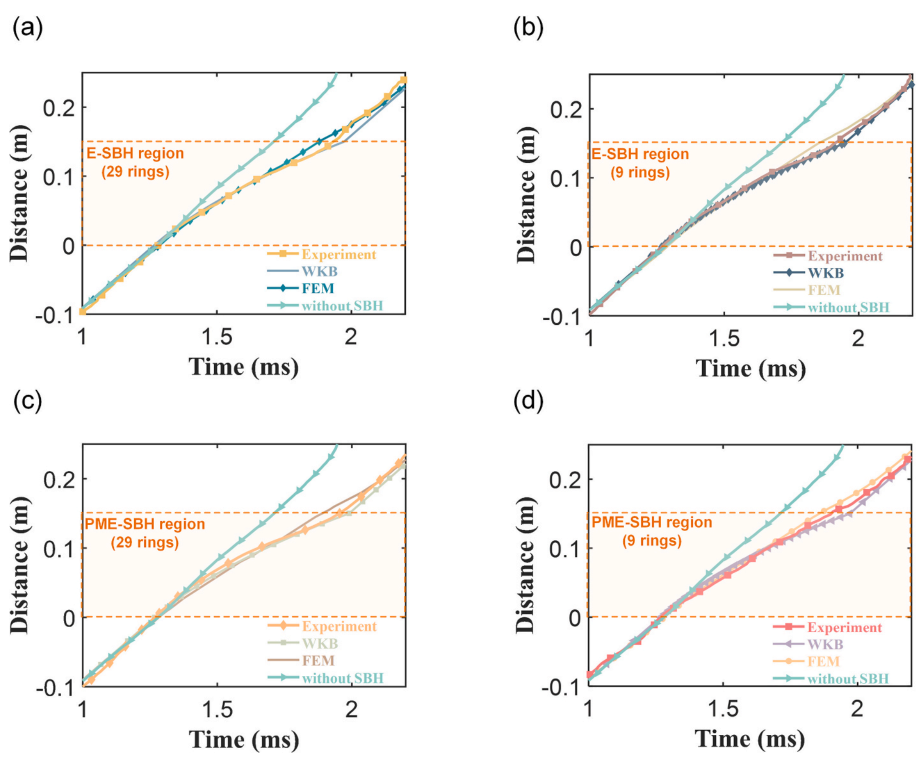

Fig. 9. Wavefront location versus time curves for (a) the 29-ring E-SBH model, (b) the 9-ring E-SBH model, (c) the 29-ring PME-SBH model, (d) the 9-ring PME-SBH model.

propagation features inside a duct with external SBH insertion. From this perspective, the reported experiments and comparisons serve the purpose. Note that using the 29-ring PME-SBH configuration, other frequencies (500 Hz and 750 Hz) were also tested, with results showing consistent and persistent slow wave effect across different frequencies (not shown here). Supported by the SBH theory (though involving simplifying assumptions) and the test results, it can be stated that the slow wave effect does exist within the frequency range where plane waves can propagate inside the duct.

5. Conclusions

In this work, the sound wave propagation characteristics inside a duct with external SBH insertion are investigated. Both bare external sonic black hole (E-SBH) and perforation-modulated external sonic black hole (PME-SBH) configurations are analyzed. Theoretical, numerical and experimental analyses are performed with a view to providing a set of useful analysis tools for the sound propagation prediction inside the ducts with comprehensive assessment in terms of slow wave features.

Four sets of WKB solutions, with clearly defined applicability ranges, are developed for predicting the sound wave propagation in both E-SBH and PME-SBH structures with continuous and discrete admittance treatments, respectively. Alongside numerical and experimental efforts, slow-wave phenomena are predicted, numerically visualized and experimentally confirmed for the external SBH configurations. It is shown that the entailed slow wave effects, characterized by the sound speed reduction and an increase of the travelling time within the SBH portion, bear a theoretical limit, mainly governed by the R_m/R_d ratio for the E-SBH configuration. For example, total travelling time is increased by 1.5 and 1.67 times, respectively, for linear and quadratic E-SBHs with $R_m/R_d = 1$. The deployment of the perforated boundary brings additional benefits by adding tunability to the SBH design. For the PME-SBH, the influence of the perforation ratio φ on the slow-wave effect overwhelms that of the hole diameter R_h. For a PME-SBH with a large number of rings investigated in the paper, φ should be selected from 10 % to 30 % to ensure the best slow wave effects. With a reduced ring number, a lower φ is imposed, typically from 5 % to 10 %. Inheriting from the previously studied conventional SBH with perforation boundary, the use of the PB in the external configuration introduces tunability into the SBH design while allowing for simpler SBH realization by reducing the number of rings without compromising the slow-wave performance.

CRediT authorship contribution statement

Sihui Li: Writing – original draft, Visualization, Validation, Software, Investigation, Data curation, Conceptualization. **Xiang Yu:** Writing – review & editing, Software, Resources, Project administration, Methodology, Formal analysis, Conceptualization. **Li Cheng:** Writing – review & editing, Supervision, Resources, Project administration, Methodology, Funding acquisition, Formal analysis.

Declaration of competing interest

The authors declare that they have no known competing financial interests or personal relationships that could have appeared to influence the work reported in this paper.

Acknowledgements

This research is supported by Research Grants Council of Hong Kong under grants No. PolyU 15201822 and N_PolyU553/23, and the National Natural Science Foundation of China (grant No. 12402106).

Data availability

Data will be made available on request.

References

[1] Mironov M. Propagation of a flexural wave in a plate whose thickness decreases smoothly to zero in a finite interval. Sov. Phys. Acoust+ 1988;34:318–9.
[2] Krylov VV. Localized acoustic modes of a quadratic solid wedge. Mosc. U. Phys. B+ 1990;45:65–9.
[3] Tang L, Cheng L, Ji H, Qiu J. Characterization of acoustic black hole effect using a one-dimensional fully-coupled and wavelet-decomposed semi-analytical model. J. Sound Vib. 2016;374:172–84. https://doi.org/10.1016/j.jsv.2016.03.031.
[4] Zhou T, Cheng L. Planar swirl-shaped acoustic black hole absorbers for multi-directional vibration suppression. J. Sound Vib. 2022;516:116500. https://doi.org/10.1016/j.jsv.2021.116500.
[5] Guasch O, Sánchez-Martín P, Ghilardi D. Application of the transfer matrix approximation for wave propagation in a metafluid representing an acoustic black hole duct termination. Appl. Math. Model. 2020;77:1881–93. https://doi.org/10.1016/j.apm.2019.09.039.
[6] Mi Y, Cheng L, Zhai W, Yu X. Broadband low-frequency sound attenuation in duct with embedded periodic sonic black holes. J. Sound Vib. 2022;536:117138. https://doi.org/10.1016/j.jsv.2022.117138.
[7] Mousavi A, Berggren M, Wadbro E. How the waveguide acoustic black hole works: A study of possible damping mechanisms. J. Acoust. Soc. Am. 2022;151:4279. https://doi.org/10.1121/10.0011788.
[8] Mironov M, Pislyakov V. One-dimensional sonic black holes: Exact analytical solution and experiments. J. Sound Vib. 2020;473:115223. https://doi.org/10.1016/j.jsv.2020.115223.
[9] Sheng H, He M-X, Lee H, Ding Q. Quasi-periodic sonic black hole with low-frequency acoustic and elastic bandgaps. Compos. Struct. 2024;337:118046. https://doi.org/10.1016/j.compstruct.2024.118046.
[10] Mi Y, Zhai W, Cheng L, Xi C, Yu X. Wave trapping by acoustic black hole: Simultaneous reduction of sound reflection and transmission. Appl. Phys. Lett. 2021;118:114101. https://doi.org/10.1063/5.0042514.
[11] Červenka M, Bednařík M. On the role of resonance and thermoviscous losses in an implementation of "acoustic black hole" for sound absorption in air. Wave Motion 2022;114:103039. https://doi.org/10.1016/j.wavemoti.2022.103039.
[12] Zhang X, He N, Cheng L, Yu X, Zhang L, Hu F. Sound absorption in sonic black holes: Wave retarding effect with broadband cavity resonance. Appl. Acoust. 2024;221:110007. https://doi.org/10.1016/j.apacoust.2024.110007.
[13] Mironov M, Pislyakov V. One-dimensional acoustic waves in retarding structures with propagation velocity tending to zero. Acoust. Phys+ 2002;48:347–52. https://doi.org/10.1134/1.1478121.
[14] Li S, Yu X, Cheng L. Enhancing wave retarding and sound absorption performances in perforation-modulated sonic black hole structures. J. Sound Vib. 2025;596:118765. https://doi.org/10.1016/j.jsv.2024.118765.
[15] Liang X, Liang H, Chu J, Wang W, Li N, Yang Z, et al. A modified sonic black hole structure for improving and broadening sound absorption. Appl. Acoust. 2023;210:109440. https://doi.org/10.1016/j.apacoust.2023.109440.
[16] Peng L, Mao Q, Wang H, Lai L, Shi Q, Chen M. Enhanced sound absorption with the combined sonic black holes. Appl. Acoust. 2024;219:109932. https://doi.org/10.1016/j.apacoust.2024.109932.
[17] Serra G, Guasch O, Arnela M, Miralles D. Optimization of the profile and distribution of absorption material in sonic black holes. Mech. Syst. Signal Pr. 2023;202:110707. https://doi.org/10.1016/j.ymssp.2023.110707.
[18] Deng J, Guasch O. Sound waves in continuum models of periodic sonic black holes. Mech. Syst. Signal Pr. 2023;205:110853. https://doi.org/10.1016/j.ymssp.2023.110853.
[19] Ou Y, Zhao Y. Design, analysis, and experimental validation of a sonic black hole structure for near-perfect broadband sound absorption. Appl. Acoust. 2024;225:110196. https://doi.org/10.1016/j.apacoust.2024.110196.
[20] Zhang X, Cheng L. Broadband and low frequency sound absorption by Sonic black holes with Micro-perforated boundaries. J. Sound Vib. 2021;512:116401. https://doi.org/10.1016/j.jsv.2021.116401.
[21] Chen Y, Yu K, Fu Q, Zhang J, Lu X. Modeling and analytical solution of an ideal continuum sonic black hole. Appl. Math. Model. 2025;141:115903. https://doi.org/10.1016/j.apm.2024.115903.
[22] Chen Y, Yu K, Fu Q, Zhang J, Lu X. Modification of the transfer matrix method for the sonic black hole and broadening effective absorption band. Mech. Syst. Signal Pr. 2024;220:111660. https://doi.org/10.1016/j.ymssp.2024.111660.
[23] Liang X, Liang H, Chu J, Jin F, Wu J. Sound absorber based on a sonic black hole and multi-layer micro-perforated panels. Phys. Scr. 2024;99:065960. https://doi.org/10.1088/1402-4896/ad478a.
[24] Peng L, Mao Q. Helmholtz resonator with sonic black hole neck. Int. J. Acoust. Vib. 2023;28:460–8. https://doi.org/10.20855/ijav.2023.28.42006.
[25] Deng J, Guasch O, Ghilardi D. Solution and analysis of a continuum model of sonic black hole for duct terminations. Appl. Math. Model. 2024;129:191–206. https://doi.org/10.1016/j.apm.2024.01.046.
[26] Umnova O, Brooke D, Leclaire P, Dupont T. Multiple resonances in lossy acoustic black holes - theory and experiment. J. Sound Vib. 2023;543:117377. https://doi.org/10.1016/j.jsv.2022.117377.

[27] Yu Y-H, Huang W, Xie L-X, Li Z-H, Li X, Lu M-H. Broadband sound absorption and slow wave in truncated sonic black hole. Appl. Acoust. 2025;235:110677. https://doi.org/10.1016/j.apacoust.2025.110677.

[28] Hruška V, Groby J-P, Bednařík M. Complex frequency analysis and source of losses in rectangular sonic black holes. J. Sound Vib. 2024;571:118107. https://doi.org/10.1016/j.jsv.2023.118107.

[29] Červenka M, Bednařík M. Numerical study of the behavior of rectangular acoustic black holes for sound absorption in air. Wave Motion 2023;123:103230. https://doi.org/10.1016/j.wavemoti.2023.103230.

[30] Bednarik M, Cervenka M. A sonic black hole of a rectangular cross-section. Appl. Math. Model. 2024;125:529–43. https://doi.org/10.1016/j.apm.2023.09.005.

[31] Červenka M, Bednařík M. Maximizing the absorbing performance of rectangular sonic black holes. Appl. Sci. 2024;14:7766. https://doi.org/10.3390/app14177766.

[32] Chen Y, Yu K, Fu Q, Zhang J, Lu X, Du X, et al. A broadband and low-frequency sound absorber of sonic black holes with multi-layered micro-perforated panels. Appl. Acoust. 2024;217:109817. https://doi.org/10.1016/j.apacoust.2023.109817.

[33] Chua JW, Li X, Yu X, Zhai W. Novel slow-sound lattice absorbers based on the sonic black hole. Compos. Struct. 2023;304:116434. https://doi.org/10.1016/j.compstruct.2022.116434.

[34] Li S, Xia J, Yu X, Zhang X, Cheng L. A sonic black hole structure with perforated boundary for slow wave generation. J. Sound Vib. 2023;559:117781. https://doi.org/10.1016/j.jsv.2023.117781.

[35] Mao Q, Peng L. Broadband and high-efficiency acoustic energy harvesting with loudspeaker enhanced by sonic black hole. Sensor. Actuat. A-Phys. 2024;379:115888. https://doi.org/10.1016/j.sna.2024.115888.

[36] Li Y, Li L, Xiao L, Cheng L, Yu X. Enhancing ventilation window acoustics with sonic black hole integration: A performance evaluation. Appl. Acoust. 2025;229:110388. https://doi.org/10.1016/j.apacoust.2024.110388.

[37] Bravo T, Maury C. Broadband sound attenuation and absorption by duct silencers based on the acoustic black hole effect: Simulations and experiments. J. Sound Vib. 2023;561:117825. https://doi.org/10.1016/j.jsv.2023.117825.

[38] Sharma N., Umnova O., Moorhouse A., Low frequency sound absorption through a muffler with metamaterial lining, in: International Congress on Sound and Vibration, London, United Kingdom 2017.

[39] Bravo T, Maury C. Converging rainbow trapping silencers for broadband sound dissipation in a low-speed ducted flow. J. Sound Vib. 2024;589:118524. https://doi.org/10.1016/j.jsv.2024.118524.

[40] Maury C, Bravo T, Amielh M, Mazzoni D. Acoustic pressure amplification through in-duct sonic black holes. Appl. Sci. 2024;14:4699. https://doi.org/10.3390/app14114699.

[41] Atalla N, Sgard F. Modeling of perforated plates and screens using rigid frame porous models. J. Sound Vib. 2007;303:195–208. https://doi.org/10.1016/j.jsv.2007.01.012.